



Influence of anthropogenic greenhouse gases on the propensity for nocturnal cold-air drainage

David E. Rupp¹ · Sarah L. Shafer² · Christopher Daly³ · Julia A. Jones⁴ · Chad W. Higgins⁵

Received: 4 March 2021 / Accepted: 27 June 2021 / Published online: 29 July 2020

© The Author(s), under exclusive licence to Springer-Verlag GmbH Austria, part of Springer Nature 2021

Abstract

Cold-air drainage and pooling can have wide-ranging impacts, including affecting ecosystem processes and agricultural crops, and contributing to decreased air quality associated with temperature inversions. Future climate changes may alter both the frequency and intensity of cold-air drainage. This study estimates the response of nocturnal cold-air drainage to warming resulting from anthropogenic greenhouse gases, specifically CO₂, considering radiative and thermodynamic effects but not changes in background air flow (dynamic effects). A simple index is proposed to represent the propensity for clear-sky nocturnal cold-air drainage as a function of air temperature and humidity near dusk. Decreases in this index with increasing atmospheric emissivity due to increasing anthropogenic greenhouse gas concentrations imply a weakening of cold-air drainage. The magnitude of the decrease in the index is positively related to the initial background temperature and humidity: Warm regions are more sensitive than cold regions, and humid regions are more sensitive than dry regions, implying that warm and/or humid regions are more at risk of decreases in cold-air drainage. Under atmospheric CO₂ concentrations consistent with Representative Concentration Pathway (RCP) 8.5, the magnitude of decrease in the index indicates that nocturnal cold-air drainage intensity may decline by at least 10% by 2100 CE (compared to 1979–1990) with larger decreases in warm and humid regimes. The index should be tested with intentionally designed field or lab experiments, and the relative effects on cold-air drainage of changes in radiative, sensible, and latent heat fluxes, and atmospheric circulation, should be compared.

1 Introduction

Cold-air drainage down hillslopes and the resulting cold-air pooling in valleys and depressions are common meteorological phenomena (Whiteman et al. 2004; Vitasse et al. 2017; Jemmett-Smith et al. 2018; Miró et al. 2018; Kelsey et al. 2019; Joly and Richard 2019). Cold-air drainage develops when a net positive upward radiative flux at the surface

initiates cooling of near-surface air on a sloping surface. If this cooling air consequently achieves a density greater than that of the air farther from the surface but at similar altitude, the near-surface air will move downslope. Warmer air replaces the displaced air, subsequently cools, and itself drains. The draining air may continue downslope until it reaches a surface barrier or constriction, it may accumulate above previously drained air, forming a cold-air pool (Marvin 1914; Burns and Chemel 2014) or the drainage may be interrupted by local dynamical processes related to the draining flow itself (e.g., Jemmett-Smith et al. 2019). Cold-air drainage and pooling is driven by many factors, including local radiative, sensible and latent heat fluxes, surface roughness, canopy cover, and synoptic-scale atmospheric circulation that drives local winds, vapor transport, cloud cover, and precipitation (e.g., Pepin et al. 2011). Clear skies and the absence of solar radiation can result in the radiative conditions necessary to produce cold-air drainage, while other favorable meteorological factors include light winds and a stable atmosphere (Barr and Orgill 1989; Daly et al. 2010; Jemmett-Smith et al. 2018).

✉ David E. Rupp
david.rupp@oregonstate.edu

¹ Oregon Climate Change Research Institute, College of Earth, Ocean, and Atmospheric Sciences, Oregon State University, Corvallis, OR, USA

² U.S. Geological Survey, Corvallis, OR, USA

³ PRISM Climate Group, Northwest Alliance for Computational Science and Engineering, College of Engineering, Oregon State University, Corvallis, OR, USA

⁴ Geography, College of Earth, Ocean, and Atmospheric Sciences, Oregon State University, Corvallis, OR, USA

⁵ Department of Biological and Ecological Engineering, Oregon State University, Corvallis, OR, USA

Cold-air drainage and pooling affects carbon fluxes (Pypker et al. 2007; Novick et al. 2016), snow and ice melt (Whiteman et al. 2001), and habitat for flora and fauna (Dobrowski 2011; Lenoir et al. 2017). Persistent cold-air pools (e.g., lasting at least one diurnal cycle) can lead to poor air quality and to hazards associated with fog and freezing rain (e.g., see review in Reeves and Stensrud 2009). Despite the importance of cold-air drainage to biological and physical processes, little has been published on how climate change might affect cold-air drainage. Daly et al. (2010) considered how climate warming together with an increase in the synoptic-scale atmospheric conditions positively associated with cold-air drainage could affect spatial patterns of temperature distribution across a small mountain basin. However, Daly et al. (2010) did not address whether warming driven by anthropogenic greenhouse gases (AGHGs) would actually increase, or decrease, such synoptic-scale atmospheric conditions. Ji et al. (2019) found a strengthening of simulated near-surface inversions over southeast Australia under projected global warming, but did not isolate the role that changes in cold-air drainage had on inversions. Much uncertainty remains in how factors that influence cold-air drainage, particularly synoptic-scale atmospheric dynamics, will respond to AGHGs at a given location (Collins et al. 2013).

To our knowledge, no studies have examined how AGHGs might directly affect the frequency or magnitude of cold-air drainage. To assess the potential sensitivity of cold-air drainage to changing AGHG concentrations, we develop an index of cold-air drainage propensity and apply the index to estimate possible responses of cold-air drainage to AGHG changes under various conditions of moisture and temperature. Our theoretical analysis considers only the direct radiative effects on cold-air drainage from AGHG-driven background warming.

2 Methods

2.1 Deriving a simple radiation-based index for cold-air drainage propensity

We consider only clear-sky conditions because clear skies strongly promote the development of nocturnal cold-air drainage (Barr and Orgill 1989) and this assumption simplifies the radiative balance. Under clear skies, the long-wave downwelling radiative flux R_{LD} (W m^{-2}) at the surface is often approximated by

$$R_{LD} = \epsilon \sigma T_s^4 \quad (1)$$

where ϵ is effective atmospheric emissivity (e.g., Brutsaert 1975), T_s is the air temperature measured near the ground

surface (though not immediately above it, a distinction whose importance will be made clearer in Sect. 2.2), and σ is the Stefan-Boltzmann constant ($5.6703\text{E-}8 \text{ W m}^{-2} \text{ K}^{-4}$). The long-wave upwelling radiative flux R_{LU} (W m^{-2}) can be similarly calculated from the surface emissivity ϵ_{surf} (Wilber et al. 1999) and surface temperature T_{surf} by

$$R_{LU} = \epsilon_{surf} \sigma T_{surf}^4 \quad (2)$$

At local dusk, defined as time $t=0$, or the moment when the short-wave downwelling (and upwelling) radiative flux at the surface becomes negligible, there is normally an imbalance between the downwelling long-wave and the upwelling long-wave radiative fluxes at the surface, such that $R_{LU} > R_{LD}$.

We suggest that an index of the potential, or propensity, for cold-air drainage to develop at night can be derived from the difference between the air temperature at dusk ($T_{s,0}$) and what T_{surf} would need to be to instantaneously achieve long-wave balance: $R_{LU}=R_{LD}$. The hypothetical surface temperature required to instantaneously achieve radiative equilibrium, which we call the *instantaneous equilibrium surface temperature at t=0*, $T_{surf,eq}$, is solved for by equating Eq. (1) and (2) and substituting $T_{surf,eq}$ for T_{surf} :

$$T_{surf,eq} = \left(\frac{\epsilon}{\epsilon_{surf}} \right)^{1/4} T_{s,0} \quad (3)$$

Clearly, the surface temperature will not reach $T_{surf,eq}$ under realistic transient nighttime conditions because R_{LD} will change through time and R_{LU} will respond to changes in sensible, latent, and ground heat fluxes as they adjust to achieve radiative balance.

Despite the preceding caveat, $T_{surf,eq} \ll T_{s,0}$ implies high potential for the surface to cool to a temperature lower than the air temperature above it and therefore high potential for a thin layer of air to form immediately above the surface that is colder than the background air. Using, therefore, the difference $T_{s,0} - T_{surf,eq}$ as a measure of the potential for cold-air drainage to develop, we propose the following dimensionless *simple radiation-based index for cold-air drainage propensity*, ψ :

$$\psi = [(T_{s,0} - T_{surf,eq}) / T_{s,0}]^{1/2} \quad (4)$$

A high value of ψ implies a potential for the surface, and therefore the air immediately above it, to cool rapidly. Motivation for the exponent 1/2 is given in Sect. 2.2.

The index ψ can also be expressed in terms of potential temperature θ , which is advantageous because potential temperature provides a more direct measure of the vertical stability of air at the ground surface with respect to air

at temperature $T_{s,0}$ by bringing $T_{s,0}$ to the surface pressure $P_{surf,0}$ adiabatically. Replacing temperature with potential temperature in Eq. (4) yields

$$\psi = [(\theta_{s,0} - T_{surf,eq})/\theta_{s,0}]^{1/2} \quad (5)$$

where

$$\theta_{s,0} = T_{s,0}(P_{surf,0}/P_{s,0})^{R_d/c_p} \quad (6)$$

where R_d is the gas constant for dry air ($287.053 \text{ J kg}^{-1} \text{ K}^{-1}$), c_p is the specific heat of dry air ($1000 \text{ J kg}^{-1} \text{ K}^{-1}$), and $P_{s,0}$ is the pressure level (hPa) at $T_{s,0}$. Note that because $T_{surf,eq}$ is not an air temperature, it does not make strict sense to express it with an equivalent potential temperature (see Online Resource Appendix S1).

Clearly, the index ψ is essentially a function of effective atmospheric emissivity if it is expressed in terms of the ratio of the effective atmospheric emissivity to the surface emissivity, which is shown by substituting Eq. (3) into Eq. (4) to yield

$$\psi = \left[1 - (\epsilon/\epsilon_{surf})^{1/4} \right]^{1/2} \quad (7)$$

Using potential temperature in place of temperature in Eqs. (3) and (4), the index can be expressed as follows:

$$\psi = \left[1 - (\epsilon/\epsilon_{surf})^{1/4} (P_{s,0}/P_{surf,0})^{R_d/c_p} \right]^{1/2} \quad (8)$$

In practice, using potential temperature matters more when $P_{s,0}$ or $P_{surf,0}$ are markedly different. For this study, we assume a thin draining air layer such that Eqs. (4) and (5) or Eqs. (7) and (8) would give similar results.

2.2 Cold-air drainage propensity index and downslope flow velocity

Here, we provide the motivation for the functional form of ψ given by Eqs. (4) and (5). Assume a thin layer of air with thickness h directly above a surface with a slope angle α . Furthermore, assume that the potential temperature outside the layer is θ_a (i.e., the background temperature) and the potential temperature within the layer is θ_l . The ratio $(\theta_a - \theta_l)/\theta_a$ is a measure of the buoyant force that drives air to move downslope at velocity u (Mahrt 1982). Mahrt (1982) showed how a downslope flow velocity under idealized equilibrium conditions (\hat{u}) can be estimated using

$$u^* = \frac{\hat{u}}{[hg \sin \alpha / (C_D + k)]^{1/2}} = \left[\frac{(\theta_a - \theta_l)}{\theta_a} \right]^{1/2} \quad (9)$$

where g is the acceleration due to gravity, C_D is the drag coefficient, k is a mixing or entrainment coefficient, and u^*

is the downslope velocity expressed in dimensionless form. Although not explicitly shown, both C_D and k are themselves functions of \hat{u} , while the thickness of the layer h may be affected by the atmospheric stability. The development of the drainage layer may also affect the background flow and thus the vertical mixing, which can serve to weaken or disrupt the flow (e.g., Jemmett-Smith et al. 2019). However, for simplicity, we assume that the rate of change $d[h/(C_D + k)]/du$ is much smaller than $d[(\theta_a - \theta_l)/\theta_a]/du$ and thus treat $h/(C_D + k)$ as a constant. Clearly, Eq. (9) represents an idealized hillslope, whereas the development of cold-air drainage will be different for different terrain, such as shallow basins (e.g., Gustavsson et al. 1998) and deep valleys (e.g., Arduini et al. 2016, 2017). Local details (e.g., land cover) will influence the manner and extent to which a change in radiative cooling alone determines a change in the maximum flow strength (Burns and Chemel 2014).

Based on Eq. (9), we assume that u^* is positively related to our index ψ . That is, when ψ is larger, the asymptotically maximum downslope velocity achievable during the night is also likely to be larger. More specifically, we assume that relative changes in u^* with increasing background air temperature are approximately equal to the relative changes in ψ with increasing background air temperature:

$$\frac{1}{\psi} \frac{\partial \psi}{\partial \theta_{a,0}} \approx \frac{1}{u^*} \frac{\partial u^*}{\partial \theta_a} \quad (10)$$

We emphasize that we do not claim that $(\theta_{s,0} - T_{surf,eq})/\theta_{s,0}$ from Eq. (5) can substitute for $(\theta_a - \theta_l)/\theta_a$ in Eq. (9) to predict u^* . First, $(\theta_{s,0} - T_{surf,eq})/\theta_{s,0}$ does not express an existing relative temperature difference, but a hypothetical difference that would exist if the surface equilibrated instantaneously to a given temperature $T_{s,0}$ (with corresponding potential temperature $\theta_{s,0}$). Instead, $(\theta_{s,0} - T_{surf,eq})/\theta_{s,0}$ can be viewed as a *potential* (what we call *propensity* to not confuse it with the “potential” in potential temperature) for cold-air drainage to occur due to long-wave cooling.

Second, θ_l in Eq. (9) is the air temperature in the draining layer, whereas $T_{surf,eq}$ is a hypothetical temperature of the surface. Although the surface temperature will influence the air temperature through the exchange of mass (moisture) and energy (e.g., Sun et al. 2005), they need not be identical. Under clear skies, the surface is typically warmer than the air temperature 1 to 3 m above it during the day and cooler at night, with a transition from warmer to colder occurring shortly before sunset (Jin et al. 1997; Edwards et al. 2011; Good 2016). Because the surface typically cools faster than the air above it during the evening, our index of a hypothetical buoyant force, $(\theta_{s,0} - T_{surf,eq})/\theta_{s,0}$, will underestimate the buoyant force when the surface is colder than the adjacent air, so a more precise expression would be $[\theta_{s,0} - (T_{surf,eq} + \Delta)]/\theta_{s,0}$, where Δ is the difference between

$T_{surf,eq}$ and the associated potential temperature of the air immediately above it. The effect of Δ will be negligible if $(\theta_{s,0} - T_{surf,eq}) \gg \Delta$, or if the following condition holds true:

$$\frac{\epsilon}{\epsilon_{surf}} \ll \left(\frac{T_{s,0} - \Delta}{T_{s,0}} \right)^4 \quad (11)$$

(see Online Resource Appendix S1 for the derivation of Eq. (11)). For a typical condition near dusk where $\Delta = 2$ K (e.g., Good 2016) and $T_{s,0} = 298$ K, $\epsilon/\epsilon_{surf} \ll 0.973$, showing how the index becomes less valid as ϵ approaches ϵ_{surf} . Consequently, our propensity index will approach zero less quickly as ϵ increases than if we had included the effect of Δ .

2.3 Sensitivity of the cold-air drainage propensity index to AGHG-driven warming

When considering the effect of anthropogenic AGHG-driven warming on the cold-air drainage propensity index, it is clear from Eq. (7) that the primary term of interest here is the effective atmospheric emissivity. We assume surface emissivity does not change, although it can vary with changes in land use, land cover, and snow cover. We can estimate effective atmospheric emissivity from Brutsaert (1975) who derived a commonly used formula for clear-sky R_{LD} based on simplifying assumptions for the vertical profiles of temperature and water vapor (Online Resource Appendix S2):

$$\frac{R_{LD}}{\sigma T_s^4} = \epsilon_B = \lambda(e_s/T_s)^m \quad (12)$$

where ϵ_B is the “Brutsaert emissivity”, e_s is the ground-level vapor pressure, m is an empirically derived constant, and the parameter λ is a function of both T_s and the change in air temperature T with height z , or lapse rate $\Gamma = -dT/dz$ (Online Resource Appendix S3). Brutsaert (1975) assumed $m = 1/7$ and held λ constant based on its relatively low sensitivity to changes in T_s and Γ . Although many formulas exist for estimating clear-sky R_{LD} (see reviews in Prata 1996; Flerchinger et al. 2009; Guo et al. 2019), Eq. (12) is convenient because it provides an analytical expression for emissivity as a function of three local factors that are predicted to change with increasing AGHG concentrations: T_s , e_s , and Γ (e.g., Ramanathan et al. 1979). Equation (12) is also well tested and has been found to perform as well as, if not better than, other formulas in a variety of tropical (e.g., Culf and Gash 1993; Duarte et al. 2006), temperate (e.g., Flerchinger et al. 2009), and Arctic (e.g., Sedlar and Hock 2009) settings. However, we acknowledge that the universality of the functional form of Eq. (12), and that of all common formulas using surface meteorological conditions, is questionable (Abramowitz et al. 2012).

Equation (12) underestimates effective emissivity at low vapor pressure because ϵ_B goes to zero as e_s goes to zero, yet in reality the atmosphere’s effective emissivity would remain > 0 due to the presence of other emitting gases (Konzelmann et al. 1994; Prata 1996). We therefore limit ϵ_B to a lower “background” emissivity value ϵ_0 . Considering CO₂ only, ϵ_0 has a calculated range of 0.176–0.185 at mean sea level (m.s.l.) at 300 ppm CO₂ (Prata 1996). Observation-based published values of ϵ_0 considering all atmospheric gases range from 0.20–0.23 (e.g., Dürr and Philipona 2004); we assume $\epsilon_0 = 0.2$ at m.s.l.

Although Eq. (12) can be used to estimate the effect on local R_{LD} due to local temperature and humidity changes arising from increasing AGHG concentrations, it cannot be used as is to estimate the *direct radiative effect* of additional AGHGs on R_{LD} because the Brutsaert emissivity does not explicitly include a term for greenhouse gases. Moreover, although the formula for ϵ_B was derived from physical principles, it includes empirically derived parameters derived from a function fitted to measurements of clear-sky emissivity versus measurements of water vapor path length (Prata 1996). These measurements were taken prior to the publication of Brutsaert (1975), when the concentrations of other important long-wave emitting gases in the atmosphere, namely CO₂, were roughly at mid-twentieth century levels. The concentrations of these other gases would also have influenced the measured clear-sky emissivity of the atmosphere at a particular water vapor path length. Brutsaert’s emissivity formula, therefore, should be most valid at greenhouse gas concentrations near those at the time the measurements upon which the formula is based were taken.

We therefore add a quantity, $\Delta\epsilon_{AGHG}$, to Brutsaert’s emissivity that is the direct contribution of additional atmospheric AGHGs beyond what is taken into account by ϵ_B in Eq. (12):

$$R_{LD} = (\epsilon_B + \Delta\epsilon_{AGHG})\sigma T_s^4 \quad (13)$$

Here, we consider only the contribution of atmospheric CO₂ concentrations to $\Delta\epsilon_{AGHG}$, knowing that other greenhouse gases (e.g., CH₄, N₂O, O₃), are expected to make a lesser, but still important, combined contribution (e.g., Meinshausen et al. 2011). The contribution of CO₂ to emissivity can be expressed as the effective emissivity of CO₂ (ϵ_{CO2}) in a dry atmosphere plus an H₂O-CO₂ overlap correction (ϵ_{OL}) that considers the overlapping of H₂O and CO₂ spectral absorption bands (Staley and Jurica 1972). The direct contribution to effective emissivity from rising CO₂ concentrations after some reference time is given by

$$\Delta\epsilon_{AGHG} = \epsilon_{CO2} + \epsilon_{OL} - (\epsilon_{CO2,ref} + \epsilon_{OL,ref}) \quad (14)$$

where the effective CO₂ emissivity at the reference CO₂ concentration is $\epsilon_{CO_2,ref}$ and the H₂O-CO₂ overlap correction at the reference CO₂ concentration is $\epsilon_{OL,ref}$.

We assume the reference effective emissivity of CO₂ ($\epsilon_{CO_2,ref}$) to be 0.19 at a reference CO₂ concentration of 329 ppm (i.e., a mass mixing ratio of 5E-4 g g⁻¹) and m.s.l. (~1000 hPa) based on Staley and Jurica (1972). This atmospheric CO₂ concentration was reached circa 1973 CE, conveniently close to the Brutsaert (1975) era. By 2100 CE, the CO₂ concentration is projected to be 920 ppm under Representative Concentration Pathway (RCP) 8.5; this concentration would be reached by high rates of fossil fuel emissions compared to other published scenarios (Meinshausen et al. 2011). At 920 ppm, $\epsilon_{CO_2} = 0.213$ (Staley and Jurica 1970; Online Resource Appendix S4).

The H₂O-CO₂ overlap correction as a function of temperature and both CO₂ and H₂O optical depths is available from tables in Staley and Jurica (1970). For our purposes, calculating the H₂O-CO₂ overlap correction as a function of e_s and T_s instead of H₂O optical depth is more convenient, although this requires assumptions about the vertical temperature and humidity profiles in the troposphere. We assume the same temperature and humidity profile as Brutsaert (1975) when calculating a vertically integrated H₂O optical depth, which we use to estimate ϵ_{OL} (Online Resource Appendix S5).

Finally, we can substitute $\epsilon_B + \Delta\epsilon_{AGHG}$ for ϵ in Eqs. (7) and (8) to get both forms of the cold-air drainage propensity index accounting for the change in AGHG concentrations:

$$\psi = \left[1 - \left(\frac{\epsilon_B + \Delta\epsilon_{AGHG}}{\epsilon_{surf}} \right)^{1/4} \right]^{1/2} \quad (15a)$$

and

$$\psi = \left[1 - \left(\frac{\epsilon_B + \Delta\epsilon_{AGHG}}{\epsilon_{surf}} \right)^{1/4} \left(\frac{P_{s,0}}{P_{surf,0}} \right)^{R_d/c_p} \right]^{1/2} \quad (15b)$$

2.4 Site-specific applications of the cold-air drainage propensity index

To investigate how this sensitivity of the cold-air drainage propensity index varies geographically, we consider typical cold-air drainage conditions at three sites with contrasting climates (Table 1): (1) H.J. Andrews Experimental Forest (Cascade Range, Oregon, USA), where nocturnal cold-air drainage and subsequent cold-air pooling is most common in late summer and early fall (Daly et al. 2007; Rupp et al. 2020); (2) Kevo Subarctic Research Station located above the Arctic Circle in Finnish Lapland, where nocturnal cold-air drainage frequently commences during late afternoon in the spring and fall (Pike et al. 2013; Pike 2013); and (3) the FLONA Tapajós study area in Brazilian eastern Amazonia (da Rocha et al. 2004), where Goulden et al. (2006) observed evidence of cold-air drainage on clear nights. The effective emissivity is adjusted for the elevation at each site (Table 1; Online Resource Appendix S6).

To estimate the AGHG-driven warming effect on ψ we apply Eqs. (15a) and (15b) for a reference state ($\Delta\epsilon_{AGHG} = 0$; $T_{s,0} = T_{ref}$; $\Gamma = \Gamma_{ref}$) and a future state ($\Delta\epsilon_{AGHG} > 0$; $T_{s,0} = T_{ref} + \Delta T$; $\Gamma = \Gamma_{ref} + \Delta\Gamma$) where the reference temperature T_{ref} , reference lapse rate Γ_{ref} , temperature change ΔT , and lapse rate change $\Delta\Gamma$ vary by location (Table 1). The RCP8.5 scenario produces about a 6 K increase in mean August temperature over the northwest USA by 2100 CE compared to the 1979–1990 CE mean (Rupp et al. 2017a), averaged over simulations from the ensemble of global climate models in the Coupled Model Intercomparison Project phase 5 (CMIP5). Because projected temperature changes vary globally and seasonally, we scaled temperature changes at the Finland and Amazonia sites relative to the Oregon site (6 K increase) based on differences in the ensemble-mean CMIP5 projections (Alder et al. 2013), rounded to the nearest 0.5 K. For Finland, we used October values to avoid the larger potential impacts of snow loss on cold-air drainage in March and for eastern Amazonia we used August values (peak dry season), resulting in 5.5 and 5.0 K projected temperature increases for the two sites, respectively.

Table 1 Study site elevation, time of year, reference relative humidity (RH) range and reference air temperature ($T_{s,0}$) at dusk, projected RCP8.5 temperature change (ΔT), reference lapse rate (Γ_{ref}), and projected lapse rate change ($\Delta\Gamma$)

Location	Elevation (m)	Month	RH (%)	$T_{s,0}$ (°C)	ΔT (°C)	Γ_{ref} (°C km ⁻¹) ^d	$\Delta\Gamma$ (°C km ⁻¹)
Amazonia ^a	200	August	70–90	25	5.0	6.5	-0.5
Finland ^b	200	October	70–90	-5	5.5	6.0	-0.1
Oregon ^c	600	August	50–70	20	6.0	6.5	0.1

^aFLONA Tapajós study area in Brazilian eastern Amazonia (da Rocha et al. 2004; Goulden et al. 2006)

^bKevo Subarctic Research Station, Finland (Pike et al. 2013; Pike 2013)

^cH.J. Andrews Experimental Forest, Oregon, United States (Daly et al. 2007; Rupp et al. 2020)

^dSee Online Resource Appendix S8

Tropospheric lapse rates are projected to change with anthropogenic warming, with declines over the tropics, increases over the Arctic, and relatively little change over the mid-latitudes (Ramanathan 1977; Collins et al. 2013), though with seasonal variability (e.g., Rupp et al. 2017b). For the Amazonia site, we assume a decrease in Γ of 0.5 K km^{-1} by 2100 CE (Fig. 12.12 in Collins et al. 2013). For the Oregon and Finland sites, we assume Γ increases and decreases, respectively, on the order of 0.1 K km^{-1} (Collins et al. 2013; Rupp et al. 2017b).

We assume that relative humidity (RH) remains unchanged, as only minor changes are projected (Held and Soden 2006; Seager et al. 2010; Pierce et al. 2013). For example, over western Oregon and by the end of the twenty-first century under RCP8.5, global climate models project decreases in RH of only a few percentage points (Pierce et al. 2013). However, we discuss the implications of minor changes in RH in Sect. 3.

3 Results and discussion

3.1 Sensitivity of ψ to changes in temperature and vapor pressure only

First, we examine the sensitivity of ψ to changes in temperature and vapor pressure in the absence of changing CO₂ concentrations to separate the direct effect of CO₂ on emissivity from the effect of increasing specific humidity with increasing temperature under constant RH (i.e., the Clausius–Clapeyron equation). For now, we assume $\Gamma_{ref}=6.5 \text{ K km}^{-1}$ as did Brutsaert (1975). We find a conveniently near-linear relationship between the difference $\theta_{s,0} - T_{surf,eq}$, which we refer to as the *equilibrium temperature deficit*, and the background air temperature $\theta_{s,0}$ when RH is held constant (Online Resource Fig. S3):

$$\theta_{s,0} - T_{surf,eq} \approx c_1 \theta_{s,0} + c_0 \quad (16)$$

where c_1 and c_0 are the linear equation coefficients. Substituting Eq. (16) into Eq. (5) yields

$$\psi \approx (c_0/\theta_{s,0} + c_1)^{1/2} \quad (17)$$

for $c_0/\theta_{s,0} > -c_1$. The derivative of ψ with respect to $\theta_{s,0}$ is

$$\frac{d\psi}{d\theta_{s,0}} \approx -\frac{c_0}{2\theta_{s,0}^2(c_0/\theta_{s,0} + c_1)^{1/2}} \quad (18)$$

Thus, the relative sensitivity of ψ to a small change in $\theta_{s,0}$ can, after rearrangement of terms, be approximated by

$$-\frac{1}{\psi} \frac{\Delta\psi}{\Delta\theta_{s,0}} \approx \frac{1}{2(\theta_{s,0} - a\theta_{s,0}^2)} \quad (19)$$

where $a = -c_1/c_0$ and for $\theta_{s,0} > a\theta_{s,0}^2$. Because a is positive, the term in parentheses in the right-hand side of Eq. (19) goes to zero as $\theta_{s,0}$ goes to $1/a$ (e.g., $1/a = 321 \text{ K}$ or 48°C at $RH=70\%$); therefore, it is immediately evident that the relative sensitivity of the index increases with increasing reference air temperature.

The relative decrease in the index $-\Delta\psi/\psi$ for a 1 K increase in $\theta_{s,0}$ is small (<2%) at lower reference air temperatures (below $\sim 10^\circ\text{C}$) and at any RH (Fig. 1). This result implies that in colder regimes with their lower vapor pressure, cold-air drainage is not very sensitive to warming. At higher temperature and high RH, however, ψ rapidly becomes sensitive to warming to a point where $-\Delta\psi/\psi$ exceeds 10% for even a 1 K temperature increase. Relative decreases in ψ per K for each site are highlighted in Fig. 1 based on the reference RH and temperature at dusk given in Table 1. To place the three sites on the same figure, we used

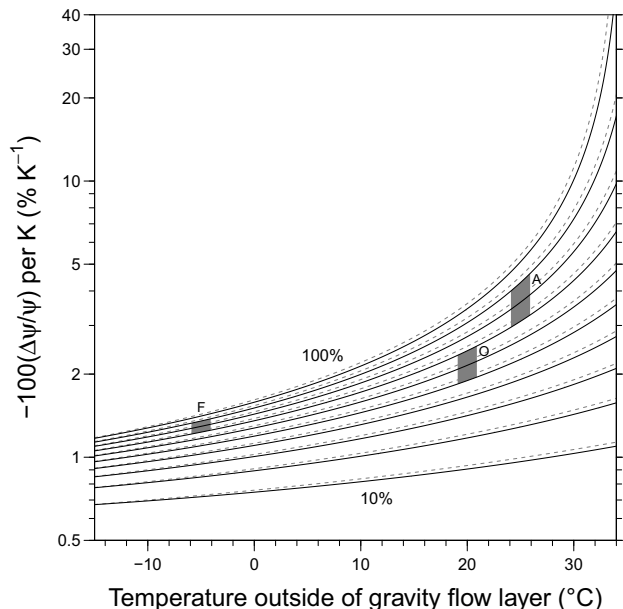


Fig. 1 Relative decrease (%) in the propensity of cold-air drainage index (ψ) per 1 K increase in the air temperature outside of the drainage layer as a function of the reference air temperature ($^\circ\text{C}$) outside of the drainage layer using the simplified approximate solution (Eq. (19); solid black lines) and full derivation (dashed gray lines; see Online Resources Appendices S1 – S5). CO₂ concentrations are constant. Solid and dashed lines show contours of constant RH ranging from 10 to 100% in 10% increments, increasing upward in the panel. Approximate representative meteorological conditions for August at the Amazonia (A) and Oregon (O) sites and October at the Finland (F) site are shown by the shaded polygons. To be able to compare all sites on the same graph, elevation and Γ_{ref} for all sites were assumed to be the same as the Oregon site (Table 1)

Fig. 2 Relative decrease (%) in the propensity of cold-air drainage index (ψ) by 2100 CE (RCP8.5) as a function of the reference air temperature (circa 1970s CE) outside of the drainage layer for the **a** Finland, **b** Oregon, and **c** Amazonia sites. A 280% increase in CO₂ concentration (920 ppm) above the circa 1970s CE reference (329 ppm) is assumed, along with local temperature and lapse rate changes given in Table 1. Solid lines include the direct emissivity effect of increased atmospheric CO₂. Gray-dashed lines exclude the direct effect of increased atmospheric CO₂ on emissivity. Both solid and dashed lines show contours of constant RH ranging from 10 to 100% in 10% increments, increasing upward in the panel. Approximate representative meteorological conditions for each site (see Table 1) are shown by the shaded polygons; darker/lighter polygons include/exclude the direct effect of increased atmospheric CO₂ on emissivity

Γ_{ref} and the elevation (which influences ψ by affecting the amount of atmosphere above the surface) of the Oregon site for all sites (Table 1) as the effect of these two factors will be small relative to the effect of site differences in reference temperature and RH. The index decreases by 3.2–4.4% K⁻¹ for the Amazonia site, 1.9–2.5% K⁻¹ for the Oregon site, and 1.3–1.4% K⁻¹ for the Finland site, at constant RH.

3.2 Sensitivity of ψ to changes in AGHG

Under the AGHG-driven warming scenario (6 K increase with a 280% increase in CO₂ concentration by 2100 CE), the index decreases by at least 10% except for conditions that are both cold (<0 °C) and very dry (<~10% RH) (Fig. 2). At the Oregon site, ψ decreases by 19%, 20%, and 23% for RH=50, 60, and 70%, respectively. As stated previously, decreases in RH of a few percentage points are projected for western Oregon and by the end of the twenty-first century under RCP8.5. Such a decrease in RH would marginally reduce the decrease in ψ .

To demonstrate the effect of $\Delta\epsilon_{AGHG}$ alone, the ψ decreases for the Oregon site described above (i.e., 19%, 20%, and 23% for RH=50, 60, and 70%) can be compared to decreases in ψ that assume the same temperature increase and associated water vapor increase but set $\Delta\epsilon_{AGHG}=0$: 12%, 13%, and 15%, respectively (Fig. 2b, dotted lines). The differences between these values with and without including $\Delta\epsilon_{AGHG}$ (e.g., 23% vs. 15% at RH=70%) reveal that the increase in the CO₂ emissivity, while smaller than the increase in the water vapor emissivity, is an important contributor to the total change in atmospheric emissivity.

To isolate the effect of the change in lapse rate from the change in temperature, we also calculated the change in ψ with $\Delta\Gamma=0$. At the Oregon site in August, the assumed increase in lapse rate would reduce the effective atmospheric emissivity and consequently reduce the decrease in ψ . However, the decrease in ψ is reduced by only a tiny fraction (<0.002) with the change in Γ imposed.

As expected given the results in Sect. 3.1 and Fig. 1, the Finland site has the smallest decreases in ψ , approximately

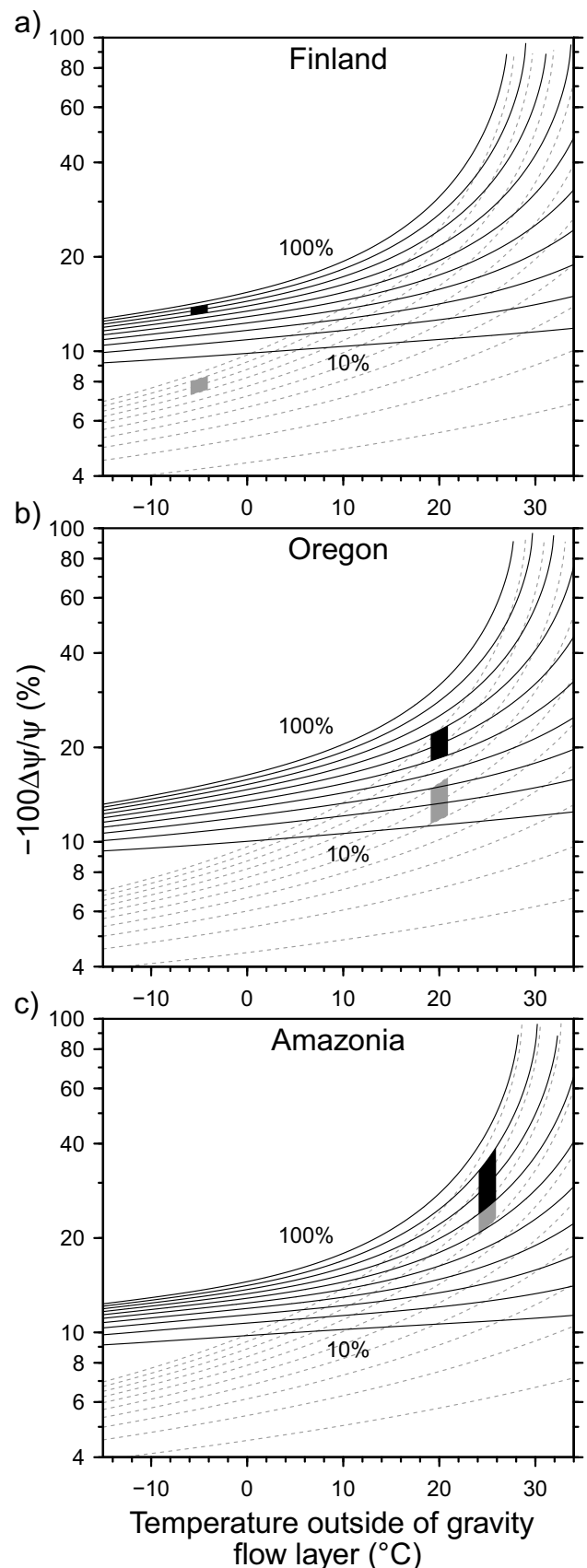


Fig. 3 Relative decrease (%) in the propensity of cold-air drainage index (ψ) by 2100 CE (RCP8.5) as a function of the reference lapse rate Γ_{ref} for the **a** Finland, **b** Oregon, and **c** Amazonia sites. Solid lines are contours of constant RH ranging from 10 to 100% in 10% increments, increasing upward in the panel. The shaded area shows the representative RH range for each site. The vertical gray line marks the value of Γ_{ref} used for Fig. 2. See Table 1 for reference conditions and projected changes in conditions assumed at each site

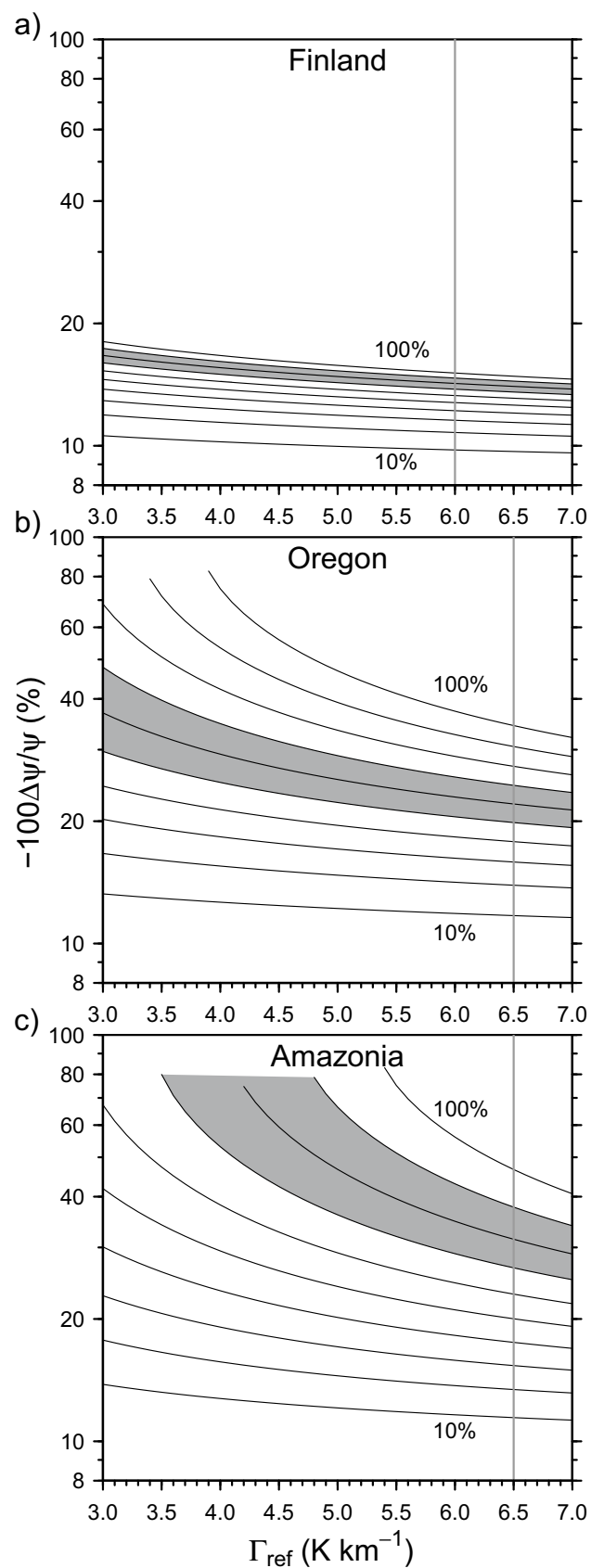
13 to 14% at RH ranging from 70 to 90%. The projected decrease in Γ adds slightly to the decrease in ψ , but the fractional contribution of the change in Γ to the change ψ is less than 0.005. In contrast, decreases in ψ at the Amazonia site are largest: 25%, 30%, and 35% for RH = 70, 80, and 90%, respectively. The projected change in Γ (-0.5 K km^{-1}) also has a small but nonnegligible effect: The fractional contribution of the change in Γ to the change in ψ ranges from 0.05 to 0.08 for RH ranging from 50 to 70%.

These relative decreases in the propensity index for the Amazonia site appear large, but they could be the result of decreases in ψ for values of ψ that are negligibly small at the start. For the reference conditions used to represent the Amazonia site, the average value of ψ is 0.17. A comparison with the Finland site where $\psi \approx 0.31$ and where cold-air drainage is frequent suggests the reference values of ψ for the Amazonia site, while smaller, are not negligible (Online Resource Appendix S7; Fig. S4).

A key result is that the sensitivity of the index to AGHG-driven warming is strongly dependent on the initial (reference) conditions. These conditions include the vertical humidity profile which is linked to the vertical temperature profile defined by Γ_{ref} (Online Resource Appendix S2). At the cold Finland site, ψ decreases are not very sensitive to Γ_{ref} (Fig. 3a). With this site's low temperatures, vapor pressures are low regardless of RH and the effective emissivity remains low regardless of Γ_{ref} , so ψ stays relatively high. Combined with a relatively low rate of change in vapor pressure with temperature (via the Clausius-Clapeyron relationship) at low temperatures, this produces small relative changes in ψ . In contrast, the warm Amazonia site is notably sensitive to Γ_{ref} with decreases in ψ from roughly 30% ($\Gamma_{ref} = 7 \text{ K km}^{-1}$) to > 80% ($\Gamma_{ref} = 4 \text{ K km}^{-1}$) for RH = 80% (Fig. 3c). Not surprisingly, the response at the Oregon site falls between the Finland and Amazonia sites, with decreases in ψ ranging from about 20 to 40% over the applied range of Γ_{ref} at RH = 60% (Fig. 3b).

3.3 Study limitations

This analysis assumes initial conditions (i.e., at dusk prior to the formation of near-surface temperature inversions resulting from cold-air drainage) of temperature and humidity decreasing with height smoothly, following Brutsaert (1975). However, actual temperature and humidity profiles at



any given time can be quite different from these hypothetical profiles. For example, lower tropospheric temperature inversions driven by synoptic-scale advection of warmer air over cooler air produce a stable atmosphere that facilitates local cold-air drainage (e.g., Reeves and Stensrud 2009; Daly et al. 2010), but such initial conditions of negative Γ in the lower troposphere cannot be explicitly produced under our assumptions. AGHG warming would still cause a decrease in ψ under such alternative initial temperature-humidity profiles, but the precise magnitude of change in ψ as a function of the reference near-surface temperature and relative humidity would depend on the relationship between these near-surface variables and the downward long-wave radiative flux that is specific to the temperature-humidity profile.

Many other factors besides changing local long-wave radiative flux may also affect the response of cold-air drainage to global climate change. Changes in atmospheric circulation, and subsequent effects on local atmospheric stability and mixing and local background winds, might suppress or promote the development of cold-air drainage and could have a larger influence than the changes in radiative fluxes examined in this study. Changes in radiative flux may also affect local stability in nonlinear ways that challenge our assumption that the index and downslope flow velocity respond similarly to changes in background air temperature (Eq. 10), although linearity may still be a reasonable approximation when background air temperature changes are limited to a few degrees C.

Further work is needed to understand how the many meteorological factors that drive cold-air drainage may change under projected future climate changes. Experiments are needed to field test and refine ψ , such as using soundings and measurements of low-level winds over a wide range of temperatures and humidity, controlled for other environmental factors. For example, soundings at dusk could be compared between days that are similar when scaled by surface temperature to determine how effectively the index predicts subsequent cold-air drainage development. Such tests could take advantage of data from existing field studies (e.g., COLPEX, Price et al. 2011; PCAPS, Lareau et al. 2013; MATERHORN, Fernando et al. 2015; SLOPE, Oldroyd et al. 2016), though small sample size and inability to control for multiple environmental factors will present large challenges.

4 Conclusions

We present a simple index, ψ , for the propensity of idealized nocturnal cold-air drainage to occur during calm and clear-sky conditions. The index is a function of air temperature and humidity at dusk and atmospheric CO₂

concentration. Although here we only present results for CO₂, the index may be applied for other AGHGs. We relate changes in the index due to changing atmospheric emissivity to changes in idealized downslope velocity during nocturnal cold-air drainage. Based on the index, we hypothesize that cold-air drainage intensity would decrease in a warming climate, in the absence of changes to atmospheric circulation affecting background wind flow. We further hypothesize that warm temperature regimes (either by geography or season), especially those with high relative humidity, would experience the largest relative decreases in cold-air drainage intensity. For example, warm and humid areas of the Amazon River basin would be particularly sensitive. In contrast, colder regimes would experience relatively small declines in cold-air drainage due to radiative changes alone. Assuming relative changes in ψ can be equated to relative changes in cold-air drainage (an assumption still unverified by observation), projected decreases in nocturnal cold-air drainage intensity are estimated to exceed 10% under large increases in AGHG concentrations (280% increase in CO₂) in many settings, with decreases approaching 100% in warm and humid regimes as the effective atmospheric emissivity approaches the surface emissivity. These projected changes are based only on the direct effects of AGHGs on background warming and local radiative fluxes.

Supplementary Information The online version contains supplementary material available at <https://doi.org/10.1007/s00704-021-03712-y>.

Acknowledgements We thank Nick Pepin and three anonymous reviewers for their comments. D.R. is grateful to Nick Bond for some early inspiration. Data for Oregon were provided by the H.J. Andrews Experimental Forest and Long Term Ecological Research program, administered cooperatively by the USDA Forest Service Pacific Northwest Research Station, Oregon State University, and the Willamette National Forest. Any use of trade, firm, or product names is for descriptive purposes only and does not imply endorsement by the U.S. Government.

Author's contributions Conceptualization: David Rupp and Chad Higgins. Methodology: David Rupp. Writing—original draft preparation: David Rupp; writing—review and editing: David Rupp, Sarah Shafer, Chris Daly, Julia Jones, and C. Higgins; resources: Chris Daly.

Funding David Rupp was supported by the U.S. Geological Survey (USGS; cooperative agreement G12AC20283). Sarah Shafer was supported by the USGS Climate Research and Development Program. Julia Jones and David Rupp were supported by the National Science Foundation (Andrews Forest LTER7 DEB-1440409). Chris Daly and David Rupp were supported by the U.S. Department of Agriculture Risk Management Agency (cooperative agreement 2019–2363).

Data availability The data generated for this study are available in the ScienceBase repository, <https://doi.org/10.5066/P9O32PGV> (Rupp et al. 2021).

Declarations

Conflict of interest The authors declare that they have no conflict of interest.

References

- Abramowitz G, Pouyanné L, Ajami H (2012) On the information content of surface meteorology for downward atmospheric long-wave radiation synthesis. *Geophysical Research Letters* 39:L04808. <https://doi.org/10.1029/2011GL050726>
- Alder J, Hostetler S, Williams D (2013) An interactive web application for visualizing climate data. *Eos, Transactions American Geophysical Union* 94:197–198. <https://doi.org/10.1002/2013EO220001>
- Arduini G, Chemel C, Staquet C (2017) Energetics of deep Alpine valleys in pooling and draining configurations. *J Atmos Sci* 74:2105–2124. <https://doi.org/10.1175/JAS-D-16-0139.1>
- Arduini G, Staquet C, Chemel C (2016) Interactions between the nighttime valley-wind system and a developing cold-air pool. *Boundary-Layer Meteorol* 161:49–72. <https://doi.org/10.1007/s10546-016-0155-8>
- Barr S, Orgill MM (1989) Influence of external meteorology on nocturnal valley drainage winds. *J Appl Meteor* 28:497–517. [https://doi.org/10.1175/1520-0450\(1989\)028%3c0497:IOEMON%3e2.0.CO;2](https://doi.org/10.1175/1520-0450(1989)028%3c0497:IOEMON%3e2.0.CO;2)
- Brutsaert W (1975) On a derivable formula for long-wave radiation from clear skies. *Water Resources Research* 11:742–744. <https://doi.org/10.1029/WR011i005p00742>
- Burns P, Chemel C (2014) Evolution of cold-air-pooling processes in complex terrain. *Boundary-Layer Meteorol* 150:423–447. <https://doi.org/10.1007/s10546-013-9885-z>
- Collins M, Knutti R, Arblaster J, et al (2013) Long-term climate change: projections, commitments and irreversibility. *Climate Change 2013 - The Physical Science Basis: Contribution of Working Group I to the Fifth Assessment Report of the Intergovernmental Panel on Climate Change* 1029–1136
- Culf AD, Gash JHC (1993) Longwave radiation from clear skies in Niger: a comparison of observations with simple formulas. *J Appl Meteor* 32:539–547. [https://doi.org/10.1175/1520-0450\(1993\)032%3c0539:LRFCSI%3e2.0.CO;2](https://doi.org/10.1175/1520-0450(1993)032%3c0539:LRFCSI%3e2.0.CO;2)
- da Rocha HR, Goulden ML, Miller SD et al (2004) Seasonality of water and heat fluxes over a tropical forest in eastern Amazonia. *Eco-logical Applications* 14:22–32. <https://doi.org/10.1890/02-6001>
- Daly C, Conklin DR, Unsworth MH (2010) Local atmospheric decoupling in complex topography alters climate change impacts. *International Journal of Climatology* 30:1857–1864. <https://doi.org/10.1002/joc.2007>
- Daly C, Smith JW, Smith JI, McKane RB (2007) High-resolution spatial modeling of daily weather elements for a catchment in the Oregon Cascade Mountains, United States. *J Appl Meteor Climatol* 46:1565–1586. <https://doi.org/10.1175/JAM2548.1>
- Dobrowski SZ (2011) A climatic basis for microrefugia: the influence of terrain on climate. *Global Change Biology* 17:1022–1035. <https://doi.org/10.1111/j.1365-2486.2010.02263.x>
- Duarte HF, Dias NL, Maggiotto SR (2006) Assessing daytime downward longwave radiation estimates for clear and cloudy skies in southern Brazil. *Agricultural and Forest Meteorology* 139:171–181. <https://doi.org/10.1016/j.agrformet.2006.06.008>
- Dürr B, Philipona R (2004) Automatic cloud amount detection by surface longwave downward radiation measurements. *Journal of Geophysical Research: Atmospheres* 109:D05201. <https://doi.org/10.1029/2003JD004182>
- Edwards JM, McGregor JR, Bush MR, Bornemann FJ (2011) Assessment of numerical weather forecasts against observations from Cardington: seasonal diurnal cycles of screen-level and surface temperatures and surface fluxes. *Quarterly Journal of the Royal Meteorological Society* 137:656–672. <https://doi.org/10.1002/qj.742>
- Fernando HJS, Pardyjak ER, Di Sabatino S et al (2015) The MATERHORN: unraveling the intricacies of mountain weather. *Bull Amer Meteor Soc* 96:1945–1967. <https://doi.org/10.1175/BAMS-D-13-00131.1>
- Flerchinger GN, Xao W, Marks D et al (2009) Comparison of algorithms for incoming atmospheric long-wave radiation. *Water Resources Research* 45:W03423. <https://doi.org/10.1029/2008WR007394>
- Good EJ (2016) An in situ-based analysis of the relationship between land surface “skin” and screen-level air temperatures. *Journal of Geophysical Research: Atmospheres* 121:8801–8819. <https://doi.org/10.1002/2016JD025318>
- Goulden ML, Miller SD, da Rocha HR (2006) Nocturnal cold air drainage and pooling in a tropical forest. *Journal of Geophysical Research: Atmospheres* 111:D08S04. doi:<https://doi.org/10.1029/2005JD006037>
- Guo Y, Cheng J, Liang S (2019) Comprehensive assessment of parameterization methods for estimating clear-sky surface downward longwave radiation. *Theor Appl Climatol* 135:1045–1058. <https://doi.org/10.1007/s00704-018-2423-7>
- Gustavsson T, Karlsson M, Bogren J, Lindqvist S (1998) Development of temperature patterns during clear nights. *J Appl Meteor* 37:559–571. [https://doi.org/10.1175/1520-0450\(1998\)037%3c0559:DOTPDC%3e2.0.CO;2](https://doi.org/10.1175/1520-0450(1998)037%3c0559:DOTPDC%3e2.0.CO;2)
- Held IM, Soden BJ (2006) Robust responses of the hydrological cycle to global warming. *J Climate* 19:5686–5699. <https://doi.org/10.1175/JCLI3990.1>
- Jemmett-Smith B, Ross AN, Sheridan P (2018) A short climatological study of cold air pools and drainage flows in small valleys. *Weather* 73:256–262. <https://doi.org/10.1002/wea.3281>
- Jemmett-Smith BC, Ross AN, Sheridan PF et al (2019) A case-study of cold-air pool evolution in hilly terrain using field measurements from COLPEX. *Quarterly Journal of the Royal Meteorological Society* 145:1290–1306. <https://doi.org/10.1002/qj.3499>
- Ji F, Evans JP, Di Luca A et al (2019) Projected change in characteristics of near surface temperature inversions for southeast Australia. *Clim Dyn* 52:1487–1503. <https://doi.org/10.1007/s00382-018-4214-3>
- Jin M, Dickinson RE, Vogelmann AM (1997) A comparison of CCM2–BATS skin temperature and surface-air temperature with satellite and surface observations. *Journal of Climate* 10:1505–1524. [https://doi.org/10.1175/1520-0442\(1997\)010%3c1505:ACOCBS%3e2.0.CO;2](https://doi.org/10.1175/1520-0442(1997)010%3c1505:ACOCBS%3e2.0.CO;2)
- Joly D, Richard Y (2019) Frequency, intensity, and duration of thermal inversions in the Jura Mountains of France. *Theor Appl Climatol* 138:639–655. <https://doi.org/10.1007/s00704-019-02855-3>
- Kelsey EP, Cann MD, Lupo KM, Haddad LJ (2019) Synoptic to microscale processes affecting the evolution of a cold-air pool in a northern New England forested mountain valley. *J Appl Meteor Climatol* 58:1309–1324. <https://doi.org/10.1175/JAMC-D-17-0329.1>
- Konzelmann T, van de Wal RSW, Greuell W et al (1994) Parameterization of global and longwave incoming radiation for the Greenland Ice Sheet. *Global and Planetary Change* 9:143–164. [https://doi.org/10.1016/0921-8181\(94\)90013-2](https://doi.org/10.1016/0921-8181(94)90013-2)
- Lareau NP, Crosman E, Whiteman CD et al (2013) The persistent cold-air pool study. *Bull Amer Meteor Soc* 94:51–63. <https://doi.org/10.1175/BAMS-D-11-00255.1>

- Lenoir J, Hattab T, Pierre G (2017) Climatic microrefugia under anthropogenic climate change: implications for species redistribution. *Ecography* 40:253–266. <https://doi.org/10.1111/ecog.02788>
- Mahrt L (1982) Momentum balance of gravity flows. *J Atmos Sci* 39:2701–2711. [https://doi.org/10.1175/1520-0469\(1982\)039%3c2701:MBOGF%3e2.0.CO;2](https://doi.org/10.1175/1520-0469(1982)039%3c2701:MBOGF%3e2.0.CO;2)
- Marvin CF (1914) Air drainage explained. *Mon Wea Rev* 42:583–585. [https://doi.org/10.1175/1520-0493\(1914\)42%3c583:ADE%3e2.0.CO;2](https://doi.org/10.1175/1520-0493(1914)42%3c583:ADE%3e2.0.CO;2)
- Meinshausen M, Smith SJ, Calvin K et al (2011) The RCP greenhouse gas concentrations and their extensions from 1765 to 2300. *Climatic Change* 109:213. <https://doi.org/10.1007/s10584-011-0156-z>
- Miró JR, Peña JC, Pepin N et al (2018) Key features of cold-air pool episodes in the northeast of the Iberian Peninsula (Cerdanya, eastern Pyrenees). *International Journal of Climatology* 38:1105–1115. <https://doi.org/10.1002/joc.5236>
- Novick KA, Oishi AC, Miniat CF (2016) Cold air drainage flows subsidize montane valley ecosystem productivity. *Global Change Biology* 22:4014–4027. <https://doi.org/10.1111/gcb.13320>
- Oldroyd HJ, Pardyjak ER, Higgins CW, Parlange MB (2016) Buoyant turbulent kinetic energy production in steep-slope katabatic flow. *Boundary-Layer Meteorol* 161:405–416. <https://doi.org/10.1007/s10546-016-0184-3>
- Pepin NC, Daly C, Lundquist J (2011) The influence of surface versus free-air decoupling on temperature trend patterns in the western United States. *Journal of Geophysical Research: Atmospheres* 116:D10109. <https://doi.org/10.1029/2010JD014769>
- Pierce DW, Westerling AL, Oyler J (2013) Future humidity trends over the western United States in the CMIP5 global climate models and variable infiltration capacity hydrological modeling system. *Hydrology and Earth System Sciences* 17:1833–1850. <https://doi.org/10.5194/hess-17-1833-2013>
- Pike, G. (2013) Understanding temporal and spatial temperature variation at the local scale in a high latitude environment. Doctoral dissertation, University of Portsmouth.
- Pike G, Pepin NC, Schaefer M (2013) High latitude local scale temperature complexity: the example of Kevo Valley, Finnish Lapland. *International Journal of Climatology* 33:2050–2067. <https://doi.org/10.1002/joc.3573>
- Prata AJ (1996) A new long-wave formula for estimating downward clear-sky radiation at the surface. *Quarterly Journal of the Royal Meteorological Society* 122:1127–1151. <https://doi.org/10.1002/qj.4912253306>
- Price JD, Vosper S, Brown A et al (2011) COLPEX: Field and numerical studies over a region of small hills. *Bull Amer Meteor Soc* 92:1636–1650. <https://doi.org/10.1175/2011BAMS3032.1>
- Pypker TG, Unsworth MH, Mix AC et al (2007) Using nocturnal cold air drainage flow to monitor ecosystem processes in complex terrain. *Ecological Applications* 17:702–714. <https://doi.org/10.1890/05-1906>
- Ramanathan V (1977) Interactions between ice-albedo, lapse-rate and cloud-top feedbacks: an analysis of the nonlinear response of a GCM climate model. *J Atmos Sci* 34:1885–1897. [https://doi.org/10.1175/1520-0469\(1977\)034%3c1885:IBIALR%3e2.0.CO;2](https://doi.org/10.1175/1520-0469(1977)034%3c1885:IBIALR%3e2.0.CO;2)
- Ramanathan V, Lian MS, Cess RD (1979) Increased atmospheric CO₂: Zonal and seasonal estimates of the effect on the radiation energy balance and surface temperature. *Journal of Geophysical Research: Oceans* 84:4949–4958. <https://doi.org/10.1029/JC084iC08p04949>
- Reeves HD, Stensrud DJ (2009) Synoptic-scale flow and valley cold pool evolution in the western United States. *Wea Forecasting* 24:1625–1643. <https://doi.org/10.1175/2009WAF2222234.1>
- Rupp DE, Abatzoglou JT, Mote PW (2017a) Projections of 21st century climate of the Columbia River Basin. *Clim Dyn* 49:1783–1799. <https://doi.org/10.1007/s00382-016-3418-7>
- Rupp DE, Li S, Mote PW et al (2017b) Seasonal spatial patterns of projected anthropogenic warming in complex terrain: a modeling study of the western US. *Clim Dyn* 48:2191–2213. <https://doi.org/10.1007/s00382-016-3200-x>
- Rupp DE, Shafer SL, Daly C, Jones JA, Frey SJK (2020) Temperature gradients and inversions in a forested Cascade Range basin: synoptic- to local-scale controls. *J Geophys Res Atmos* 125:e2020JD032686. <https://doi.org/10.1029/2020JD032686>
- Rupp DE, Shafer SL, Daly C, Jones JA, Higgins CW (2021) Propensity of cold air drainage index and related variables. U.S. Geological Survey data release. <https://doi.org/10.5066/P9O32PGV>
- Seager R, Naik N, Vecchi GA (2010) Thermodynamic and dynamic mechanisms for large-scale changes in the hydrological cycle in response to global warming. *J Climate* 23:4651–4668. <https://doi.org/10.1175/2010JCLI3655.1>
- Sedlar J, Hock R (2009) Testing longwave radiation parameterizations under clear and overcast skies at Storglaciären, Sweden. *The Cryosphere* 3:75–84. <https://doi.org/10.5194/tc-3-75-2009>
- Staley DO, Jurica GM (1972) Effective atmospheric emissivity under clear skies. *J Appl Meteor* 11:349–356. [https://doi.org/10.1175/1520-0450\(1972\)011%3c0349:EAEUCS%3e2.0.CO;2](https://doi.org/10.1175/1520-0450(1972)011%3c0349:EAEUCS%3e2.0.CO;2)
- Staley DO, Jurica GM (1970) Flux emissivity tables for water vapor, carbon dioxide and ozone. *J Appl Meteor* 9:365–372. [https://doi.org/10.1175/1520-0450\(1970\)009%3c0365:FETFWV%3e2.0.CO;2](https://doi.org/10.1175/1520-0450(1970)009%3c0365:FETFWV%3e2.0.CO;2)
- Sun Y-J, Wang J-F, Zhang R-H et al (2005) Air temperature retrieval from remote sensing data based on thermodynamics. *Theor Appl Climatol* 80:37–48. <https://doi.org/10.1007/s00704-004-0079-y>
- Vitasse Y, Klein G, Kirchner JW, Rebetez M (2017) Intensity, frequency and spatial configuration of winter temperature inversions in the closed La Brevine valley, Switzerland. *Theor Appl Climatol* 130:1073–1083. <https://doi.org/10.1007/s00704-016-1944-1>
- Whiteman CD, Pospichal B, Eisenbach S et al (2004) Inversion breakup in small Rocky Mountain and Alpine basins. *J Appl Meteor* 43:1069–1082. [https://doi.org/10.1175/1520-0450\(2004\)043%3c1069:IBISRM%3e2.0.CO;2](https://doi.org/10.1175/1520-0450(2004)043%3c1069:IBISRM%3e2.0.CO;2)
- Whiteman CD, Zhong S, Shaw WJ et al (2001) Cold pools in the Columbia Basin. *Wea Forecasting* 16:432–447. [https://doi.org/10.1175/1520-0434\(2001\)016%3c0432:CPITCB%3e2.0.CO;2](https://doi.org/10.1175/1520-0434(2001)016%3c0432:CPITCB%3e2.0.CO;2)
- Wilber AC, Kratz DP, Gupta SK (1999) Surface emissivity maps for use in satellite retrievals of longwave radiation. NASA TP-1999-209362. <https://ntrs.nasa.gov/api/citations/19990100634/downloads/19990100634.pdf>

Publisher's note Springer Nature remains neutral with regard to jurisdictional claims in published maps and institutional affiliations.